Seasonal changes in the vertical structure of ozone in the Martian lower atmosphere and its relationship to water vapour

Kevin Olsen[1], Anna Fedorova[2], Alexander Trokhimovskiy[3], Franck Montmessin[4], Franck Lefèvre[4], Oleg Korablev[2], Lucio Baggio[4], Francois Forget[5], Ehouarn Millour[5], Antoine Bierjon[5], Juan Alday[6], Colin Wilson[7], Patrick Irwin[1], Denis Belyaev[8], Andrey Patrakeev[2], and Alexey Shakun[2]

[1]Department of Physics, University of Oxford, Oxford, UK.
[2]Space Research Institute (IKI), Moscow, Russia.
[3]Space Research Institute (IKI)
[4]Laboratoire Atmosphères, Milieux, Observations Spatiales (LATMOS/CNRS), Paris, France.
[5]Laboratoire de Météorologie Dynamique (LMD/CNRS), Paris, France.
[6]University of Oxford
[7]European Space Research and Technology Centre,University of Oxford
[8]Space Research Institute

November 21, 2022

Abstract

The mid-infrared channel of the Atmospheric Chemistry Suite (ACS MIR) onboard the ExoMars Trace Gas Orbiter is capable of observing the infrared absorption of ozone (O3) in the atmosphere of Mars. During solar occulations, the 003-000 band (3000-3060 cm-1) is observed with spectral sampling of ˜0.045 cm-1. Around the equinoxes in both hemispheres and over the southern winters, we regularly observe around 200-500 ppbv of O3 below 30 km. The warm southern summers, near perihelion, produce enough atmospheric moisture that O3 is not detectable at all, and observations are rare even at high northern latitudes. During the northern summers, water vapour is restricted to below 10 km, and an O3 layer (100-300 ppbv) is visible between 20-30 km. At this same time, the aphelion cloud belt forms, condensing water vapour and allowing O3 to build up between 30-40 km. A comparison to vertical profiles of water vapour and temperature in each season reveals that water vapour abundance is controlled by atmospheric temperature, and H2O and O3 are anti-correlated as expected. When the atmosphere cools, over time or over altitude, water vapour condenses (observed as a reduction in its mixing ratio) and the production of odd hydrogen species is reduced, which allows O3 to build up. Conversely, warmer temperatures lead to water vapour enhancements and ozone loss. The LMD Mars Global Climate Model is able to reproduce vertical structure and seasonal changes of temperature, H2O, and O3 that we observe. However, the observed O3 abundance is larger by a factor of 2-6, indicating important differences in the rate of odd-hydrogen photochemistry.

Seasonal changes in the vertical structure of ozone in the Martian lower atmosphere and its relationship to water vapour.

K. S. Olsen[1], A. A. Fedorova[2], A. Trokhimovskiy[2], F. Montmessin[3], F. Lefèvre[3], O. Korablev[2], L. Baggio[3], F. Forget[4], E. Millour[4], A. Bierjon[4], J. Alday[1,5], C. F. Wilson[1,6], P. G. J. Irwin[1], D. A. Belyaev[2], A. Patrakeev[2], and A. Shakun[2]

[1]Department of Physics, University of Oxford, Oxford, UK.

[2]Space Research Institute (IKI), Moscow, Russia.

[3]Laboratoire Atmosphères, Milieux, Observations Spatiales (LATMOS/CNRS), Paris, France.

[4]Laboratoire de Météorologie Dynamique (LMD/CNRS), Paris, France.

[5]School of Physical Sciences, The Open University, Milton Keynes, UK.

[6]European Space Research and Technology Centre (ESTEC), Noordwijk, Netherlands

Corresponding author: Kevin S. Olsen (Kevin.Olsen@physics.ox.ac.uk)

Key Points:

- Observations of the vertical distribution of ozone on Mars over three years.
- Direct comparison of water vapour, ozone, and temperature, revealing trends and correlations.
- Ozone is observed in higher abundances than photochemical models predict.

Plain Language Summary:

Ozone on Mars is part of the so-called odd-oxygen family of reactive, oxidizing gases. It is part of many chemical cycles that help convert one type of gas into another, facilitating the transfer of carbon or hydrogen. Odd-oxygen is crucial to linking the cycles of water vapour and carbon dioxide, or the destruction of trace gases, such as methane. With the Atmospheric Chemistry Suite (ACS) onboard the ExoMars Trace Gas Orbiter (TGO), we are able to study the vertical structure of ozone in the Martian atmosphere and make direct comparisons between it and water vapour and temperature. We have observed ozone abundances several times larger than predicted, suggesting that the oxidizing power of the Martian atmosphere is stronger or faster than expected. We have also observed and measured the relationship between these products: temperature controls the abundance of water vapour, and when the atmosphere cools and water condenses, ozone is able to build up. It is the by-products of when water vapour breaks down in sunlight that remove odd-oxygen from the atmosphere.

Abstract

The mid-infrared channel of the Atmospheric Chemistry Suite (ACS MIR) onboard the ExoMars Trace Gas Orbiter is capable of observing the infrared absorption of ozone (O_3) in the atmosphere of Mars. During solar occulations, the 003←000 band (3000-3060 cm^{-1}) is observed with spectral sampling of ~0.045 cm^{-1}. Around the equinoxes in both hemispheres and over the southern winters, we regularly observe around 200-500 ppbv of O_3 below 30 km. The warm southern summers, near perihelion, produce enough atmospheric moisture that O_3 is not detectable at all, and observations are rare even at high northern latitudes. During the northern summers, water vapour is restricted to below 10 km, and an O_3 layer (100-300 ppbv) is visible between 20-30 km. At this same time, the aphelion cloud belt forms, condensing water vapour and allowing O_3 to build up between 30-40 km. A comparison to vertical profiles of water vapour and temperature in each season reveals that water vapour abundance is controlled by atmospheric temperature, and H_2O and O_3 are anti-correlated as expected. When the atmosphere cools, over time or over altitude, water vapour condenses (observed as a reduction in its mixing ratio) and the production of odd hydrogen species is reduced, which allows O_3 to build up. Conversely, warmer temperatures lead to water vapour enhancements and ozone loss. The LMD Mars Global Climate Model is able to reproduce vertical structure and seasonal changes of temperature, H_2O, and O_3 that we observe. However, the observed O_3 abundance is larger by a factor of 2-6, indicating important differences in the rate of odd-hydrogen photochemistry.

1 Introduction

Ozone (O_3) plays a crucial role in the atmospheric chemistry of Mars. First observed by the Ultraviolet Spectrometers on Mariner 7 and 9 (Barth et al., 1973; Barth & Hord, 1971), instruments on Mars Express and the ExoMars Trace Gas Orbiter (TGO) have been able to investigate its relationship with water vapour (Lefèvre et al., 2021), its vertical structure (Khayat et al., 2021; Olsen et al., 2020), and its seasonal evolution (Patel et al., 2021). Ozone is produced after the photolysis of carbon dioxide (CO_2) from molecular and atomic oxygen, and is broken down by photolysis. This latter pathway does not yield a net change in odd-oxygen (O and O_3) species, however. That most frequently occurs when atomic oxygen reacts with the hydroperoxyl radical (HO_2), a member of the odd-hydrogen family (with H and OH).

Odd-hydrogen molecules are primarily derived from water vapour photolysis and are responsible for stabilising the ratio of carbon monoxide (CO) and carbon dioxide (CO_2). A long standing problem in Martian photochemical modelling is that over long time scales the amount of CO will be underestimated (Lefèvre & Krasnopolsky, 2017). The reaction between hydroxyl (OH) and CO maintains the CO_2 mixing ratio of 95.6%. HO_2 and OH are very difficult to observe directly, but their coupling to water vapour (H_2O), which is their source molecule, and with ozone, as the odd-oxygen loss mechanism, allows the monitoring of ozone to be used as a proxy for odd-hydrogen species. Going further, a comparative study of water vapour and ozone can shed insight into several aspects of Martian photochemistry since their changing relative abundance reflect the rates of change of odd-oxygen and odd-hydrogen, which in turn control other Martian atmospheric constituents such as CO, CO_2, HCl, or nitrogen species.

The integrated column abundance of O_3 has been revealed over broad spatial areas by observations from the Earth (Espenak et al., 1991; Fast et al., 2006), the Hubble Space Telescope (Clancy et al., 1996), and by the Mars Color Imager (MARCI) onboard the Mars Reconnaissance Orbiter (Clancy et al., 2016). SPICAM (SPectroscopie pour l'Investigation des Caractéristiques Atmosphériques de Mars) on Mars Express has been able to produce both vertical profiles and

column abundances of O_3 (Lefèvre et al., 2021; Montmessin & Lefèvre, 2013; Perrier et al., 2006). The Ultraviolet and Visible Spectrometer (UVIS) channel of the Nadir and Occultation for Mars Discovery (NOMAD) instrument on TGO has been able to create a high density data set of O_3 number density vertical profiles with fine resolution (Khayat et al., 2021; Patel et al., 2021). These studies have confirmed the expected anti-correlation with water vapour, revealed a strong increase in ozone abundance over the poles during winters, and seasonality characterised by higher ozone abundances reaching to higher altitudes during the aphelion period.

The mid-infrared channel of the Atmospheric Chemistry Suite (ACS MIR) makes fine spectral resolution (separation of ~0.045 cm^{-1}) solar occultation measurements from the near-polar, circular orbit of TGO. This technique has been shown to be sensitive enough to observe the infrared absorption lines of the 003←000 absorption band of O_3 below 35 km. From the same ACS MIR observations, we can also derive coincident mixing ratios of water vapour, and from simultaneous observations of the near-infrared channel (ACS NIR), we have measurements of temperature and pressure. Herein, we investigate the vertical structure of O_3 revealed by ACS MIR and make direct comparisons with simultaneously measured vertical profiles of water vapour abundance and temperature. In the following sections we will introduce the instrument and analysis methods, present the vertical profiles of O_3, H_2O, and temperature, organised by season and latitude range, compare these results to data from the LMD Mars Global Climate Model (GCM), and discuss the quantized relationship between H_2O and O_3.

2 Materials and Methods

2.1 ACS MIR

The ExoMars Trace Gas Orbiter entered Martian orbit in late 2016, and commenced its nominal science phase in April 2018, midway through Mars year (MY) 34, and just before a global storm began as Mars approached perihelion, and summer began in the southern hemisphere. It carries four scientific instruments: a stereo camera, a neutron detector, and two spectrometer suites to study the composition of the atmosphere. The Atmospheric Chemistry Suite consists of an electronics block and three instrument channels investigating: the thermal infrared (ACS TIRVIM), the near-infrared (ACS NIR), and the mid-infrared (ACS MIR).

ACS MIR is a cross-dispersion spectrometer consisting of a large echelle diffraction grating that provides access to the infrared spectral range, coupled to a secondary diffraction grating that separates the high diffraction orders (Korablev et al., 2018). The secondary grating is steerable, and each position provides access to a specific instantaneous spectral range. Spectra are recorded on a two-dimensional detector, over which the *x*-axis corresponds to wavenumber and the *y*-axis separates the diffraction orders. Each diffraction order appears as a stripe over the detector covering around 20 rows. The width of the stripe corresponds to the vertical field of view of the instrument, so each row is a unique transmission spectrum separated by ~100 m (Korablev et al., 2018; Olsen, Lefèvre, et al., 2021; Trokhimovskiy et al., 2020). The secondary grating position used in this study is 12, which allows us to observe diffraction orders 173-192 covering the spectral range 2850-3250 cm^{-1}. This position contains the spectral features of O_3, HCl, H_2O, and CO_2, and is used in the search for CH_4.

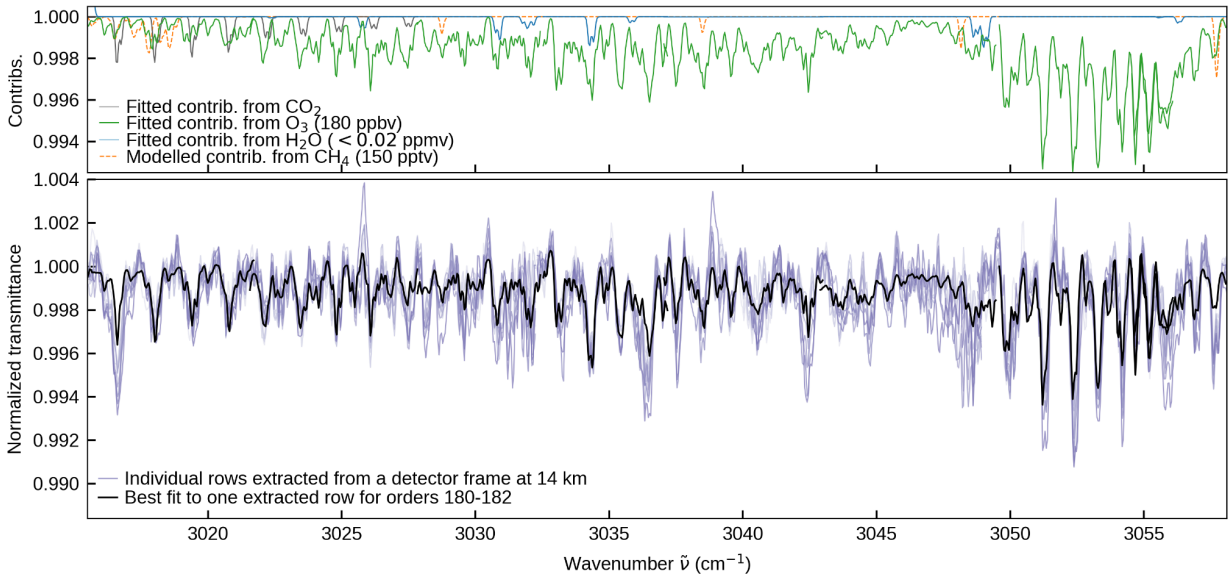

Figure 1. Example ACS MIR spectra showing ozone absorption features. Shown are normalised spectra from orders 180-182 extracted from 11 rows of the ACS MIR detector images (shades of purple) and a best-fit line for one row (black). Each row corresponds to a unique tangent height, separated by ~175 m. The top panel shows contributions to the best-fit line for different gases. The *P* and *R* branches of the 003←000 vibration rotation band are distinct and dominate the spectral range. Water vapour lines are not present and a portion of the newly-identified magnetic dipole band of CO_2 is visible at lower wavenumbers. Also indicated are the locations of CH_4 absorption lines that are targeted in this configuration of ACS MIR.

ACS MIR operates in solar occultation mode, making a series of observations of the sun while the atmosphere is between the sun and the spacecraft. Each observation is at a unique tangent height, providing a vertical resolution of 1-4 km, depending on the orbital geometry. The entire sequence of observations is analysed at once to obtain vertical profiles of the target quantities. Observations made above the top of the atmosphere provide a measurement of the solar spectrum, which is used for radiance calibration and to convert solar emission spectra into atmospheric transmission spectra. An example spectrum is shown in Figure 1 over the spectral region containing the absorption band of ozone (at wavenumbers where no sunlight is absorbed, the transmission spectra are unity).

2.2 Retrievals

Vertical profiles of the volume mixing ratio (VMR) of target gases are made using the JPL Gas Fitting Software (GFIT or GGG; Irion et al., 2002; Wunch et al., 2011). At each tangent height and over a specified spectral fitting window, a forward model is computed using volume absorption coefficients derived from the 2020 edition of the HITRAN database (Gordon et al., 2021), *a priori* VMR profiles for various gases, vertical profiles of temperature and pressure, and computed optical path through the atmosphere. Where available, line shape parameters for broadening in a CO_2-rich atmosphere are used (Devi et al., 2017; Gamache et al., 2016; Tudorie et al., 2012; Wilzewski et al., 2016). Spectral fitting is performed using non-linear Levenberg-Marquardt minimisation in which target gas VMR profiles are varied to obtain the

best-fit. Temperature and pressure data are obtained from simultaneous measurements made using the ACS NIR instrument (Fedorova et al., 2020), which observes strong CO_2 bands upwards of 90 km. *A priori* VMRs of major gases (CO_2, H_2O, O_3) were extracted from the LMD GCM with photochemistry (Lefèvre et al., 2004, 2021) at the local times of the solar terminator for the latitudes and solar longitudes (L_s) of ACS occultations. A set of estimated slant column abundances for all observed tangent altitudes is inverted with calculated slant column paths traced through the atmosphere using a linear equation solver to obtain a retrieved VMR vertical profile. This approach was previously used to study CO, O_3 and HCl with ACS MIR (Korablev et al., 2021; Olsen et al., 2020; Olsen, Lefèvre, et al., 2021).

To avoid complications due to a changing instrument line shape (Olsen, Lefèvre, et al., 2021) and to improve computational speed, several studies have been performed using ACS MIR data where a single spectrum close to the edge of the observational slit nearest the centre of the Sun was analysed at each tangent height (e.g. Alday et al., 2019; Korablev et al., 2019; Olsen et al., 2020; Trokhimovskiy et al., 2020). To improve the sensitivity of ACS MIR when absorption feature depths approach the noise level of a spectrum, such as when studying gases present in only trace amounts, or at higher altitudes, more data from the detector frame can be used. This method was developed to improve the retrievals of the trace gas hydrogen chloride (HCl) (Olsen, Trokhimovskiy, Montabone, et al., 2021), and was used to determine upper limits for phosphine (Olsen, Trokhimovskiy, Braude, et al., 2021). Each diffraction order is represented by a stripe across the detector array and upwards of 11 rows can be extracted and analysed. Each row is a unique transmission spectrum with its own tangent height (separated by only 0.1-0.2 km), line depths, noise level, and instrument line shape. Examples of 11 spectra extracted from one frame are shown in Figure 1. Sets of occultation spectra are made by grouping the spectra by row (a set of all the top-most spectra, a set of the second row, etc.), since these should have similar noise levels and instrument line shapes, and VMR vertical profile retrievals are performed on each set. The weighted average of the profiles is taken to be the best estimate of the vertical profile of the target gas VMR, and it is assigned the standard deviation of the weighted mean as an uncertainty. This method has been shown to significantly improve the accuracy of a retrieval (Olsen, Trokhimovskiy, Montabone, et al., 2021), since the impact of any data quality issues for a single spectrum are reduced (spurious features, inaccuracies when measuring quantities such as the solar spectrum, corrupted data, interpolation errors, etc.). Validation of ACS MIR data is frequently done by making comparisons of water vapour retrievals to those from ACS NIR (Fedorova et al., 2020), and this method, applied to secondary grating positions 11 and 12, has improved the stability of the ACS MIR retrievals, their accuracy, and their agreement with ACS NIR. It is used for both water vapour and ozone retrievals presented here.

3 Observations of O_3 with ACS MIR

The TGO entered Mars orbit in the fall of 2016 and began nominal science operation in April 2018 after an aerobraking campaign to circularise its near-polar orbit. Data taking with ACS MIR began on L_s 163° of MY 34 and has continued through the end of MY 35 and continues in MY 36. Opportunities for solar occultation measurements occur twice per orbit, and secondary grating position 12 is used about 15% of the time.

Figure 2 provides an overview of the ACS MIR O_3 observations. Ozone is regularly detected towards the poles, as indicated in the top panel of Figure 2, during the equinoxes (when the axial

tilt of Mars allows solar occultation to take place at the highest latitudes) and during the winters in both hemispheres when its abundance should be highest due to the cold and dry atmospheric conditions. It is never detected during southern summer due to the wet atmosphere, but is observed in northern summer, which is drier and cooler relative to the south.

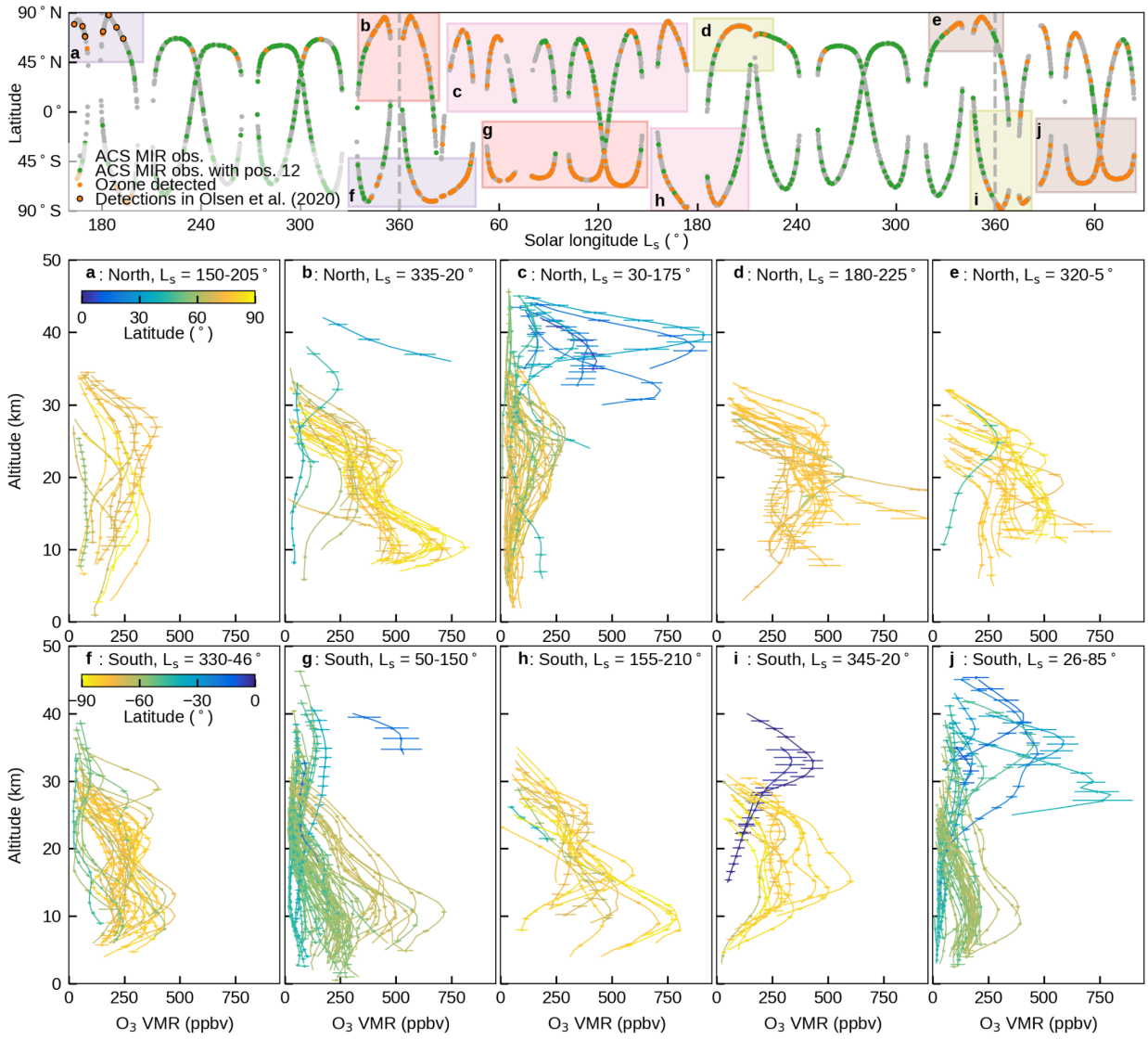

Figure 2. Overview of ozone detections with ACS MIR. The top panel shows the distribution of latitudes probed by ACS over time (solar longitude L_s) since the start of the mission on L_s 163° in Mars year (MY) 34 through to the end of MY 35 and into the beginning of MY 36. All ACS occultations are indicated in grey, those using secondary grating position 12 green, and those with 3σ ozone detections are highlighted in orange. Positive detections are grouped by L_s and latitude, and the retrieved vertical profiles are shown in the lower panels. Panels **a-e** cover the northern hemisphere, and panels **f-j** cover the southern hemisphere.

The lower panels of Figure 2 show the individual retrieved vertical profiles of O_3 VMR. Profiles are grouped by L_s in each panel, and the L_s bounds are indicated in the top panel. There are four key pieces of information that can be derived from these observations, and they are explored in

the following sections, in which we compare O_3 VMRs to retrieved water vapour abundances and temperatures. The first is that O_3 is very difficult to detect during the perihelion period, during which the atmosphere is warm, dusty, and moist in both hemispheres due to the southern summer. Detections in the northern hemisphere are rare, and ozone is not seen in the southern hemisphere. In contrast, O_3 is plentiful at all latitudes in the southern hemisphere during the aphelion period, when it is winter in the south (Figures 2**g**). Thirdly, ozone is most plentiful at high latitudes between seasons (yellow profiles in panels **b**, **d**, **e**, **f**, **h**, and **i** of Figure 2), and finally, an ozone layer near 40 km appears towards the equator during the aphelion period (blue profiles in panels **b**, **c**, **d**, **i**, and **j** in Figure 2). Figure 2 is reproduced in Figure S1 using O_3 data computed with the LMD Mars General Circulation Model (GCM), which is discussed in Section 5 (note that GCM data is only available up to the end of MY 35).

It is expected that there is great variation in O_3 VMRs between day and night, when O_3 photolysis is arrested, and TGO observations are made at either dawn or dusk. However, these diurnal changes are not evident in our data set since over any L_s period, comparing morning and evening observations necessitates a change in hemisphere as well (local times as a function of L_s are shown in the top panel of Figure 9).

The data in Figure 2**a** reproduce the results published by Olsen et al. (2020) after three major changes to the analysis method: the results are the mean of analysing 11 spectra; improved estimation of the background signal intensity; and the temperature and pressure used were updated (Fedorova et al., 2020). The shapes of the profiles remain very similar to those published previously, but with reduced uncertainties and an extension upwards from 30 to 35 km. The magnitudes of the profiles have changed, but remain around 200 ppbv. Differences are due to changes in the spectral processing (especially background light calculation) and retrieval algorithm (including the retrievals from multiple rows of the detector frame).

4 O_3 chemistry in the Martian atmosphere

The Martian atmosphere is characterised in terms of seasons similarly to Earth due to its axial tilt. For example, the northern summer solstice occurs on L_s 90°. Such seasonality is especially visible in nadir observations of its atmosphere, which have provided the dominant view of contemporary Martian climate. However, the orbital eccentricity of Mars is much larger than of Earth and its effects are dominantly visible in solar occultation observations of the vertical profiles of the Martian atmosphere (e.g., Aoki et al., 2019; Fedorova et al., 2020).

During the time period surrounding aphelion (L_s = 71°), in which it is summer in the northern hemisphere and winter in the south, minor warming over the northern pole leads to the formation of a water vapour layer near the surface (Alday et al., 2021). Extreme cooling over the south pole causes condensation of both CO_2 and water vapour on the surface. Conversely, the Martian climate in the period surrounding perihelion is driven by the spring-time sublimation of the south pole and is characterised by increased atmospheric density, the lifting of dust into the atmosphere, and a warming of the atmosphere and elevation of the hygropause. These effects are global, leading to an atmosphere above 5 km that is wetter and warmer during winter than the summer in the northern hemisphere.

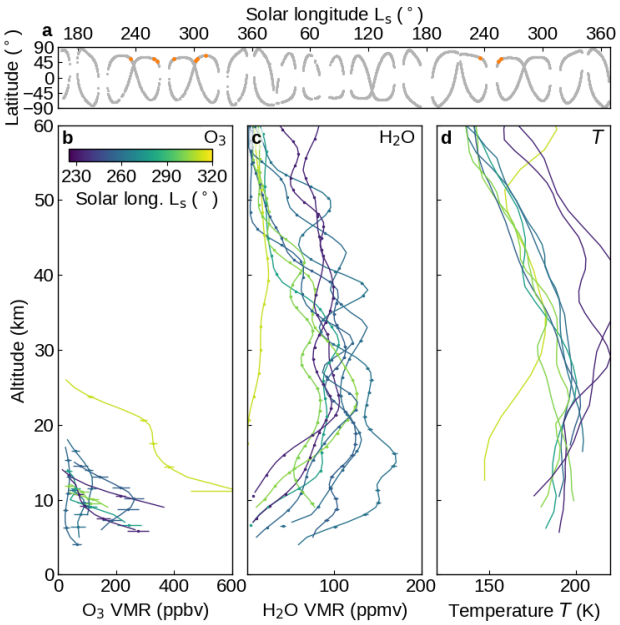

Figure 3. Perihelion ozone observations during northern winter. Panel **a** shows the latitude and L_s of observations, retrieved VMR vertical profiles of ozone (panel **b**) and water vapour (panel **c**) retrieved from ACS MIR, and temperature retrieved from ACS NIR (panel **d**). Colours indicate L_s. These profiles were measured at middle northern latitudes (45°N-66°N) around the perihelion period (northern winter).

Observations of O_3 during the perihelion result in very few O_3 detections, with limits of ~5-10 ppbv between 10-40 km. During the southern spring and summer, no observations of ozone are made at all, and during northern winter it is rarely detected; and when so, it is almost always in the presence of water vapour. Figure 3 shows the retrieved vertical profiles measured during the northern winters around perihelion of O_3 VMR from ACS MIR, H_2O VMR from ACS MIR, and temperature from ACS NIR. Water vapour is present at VMRs > 100 ppmv above 15 km, but, as these measurements are made towards polar latitudes (but south of 60°N) there is a cold layer between here and the surface (Fedorova et al., 2020) causing water to condense and the VMRs to be rapidly reduced below 20 km. This allows ACS to occasionally observe a near-polar ozone layer towards the surface with VMRs between 50-200 ppbv. A polar ozone layer over the surface is expected, but the lack of detected O_3 in most observations and the presence of H_2O suggests ACS MIR occultations are generally outside the polar vortex, which may extend south to 60°N (e.g., Mitchell et al., 2015; Waugh et al., 2016). The polar vortex is not expected to be symmetric and may be sampled irregularly by ACS MIR, depending on Ls and longitude. A notable exception occurred at L_s = 312° and 66°N. This observation reveals a substantially colder atmosphere below 30 km, with very low water vapour, resulting in 200 ppbv O_3 up to 25 km.

Southern winter observations made during the aphelion period (panel **g** in Figure 2) are shown in Figure 4, which presents vertical profiles of temperature and the VMRs of O_3 and H_2O. These profiles were recorded in the southern hemisphere at latitudes between 55°S and 66°S. In sharp contrast to the northern winter, atmospheric temperatures below 20 km are on the order of < 150 K and only rise to 165 K around 30 km. The colder atmosphere results in much lower VMRs

of water vapour by almost an order of magnitude and less than 1.5 ppmv below 20 km. At these latitudes, this allows ozone to remain in the atmosphere below 20 km. While ACS MIR solar occultations do not probe the polar nights during winters, this activity is associated with polar vortex activity, which is expected to be weaker in the southern winter than northern, cover a much broader extent, north of 50°S (Waugh et al., 2016).

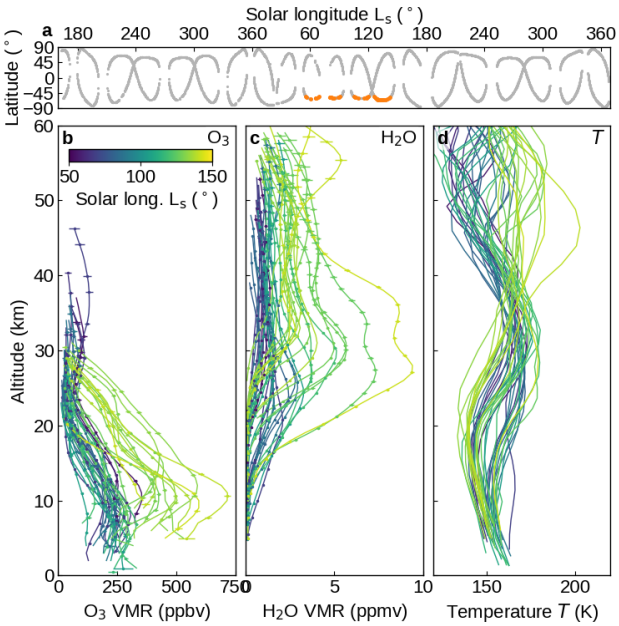

Figure 4. Aphelion ozone observations during southern winter. Panel **a** shows the latitude and L_s of observations, VMR vertical profiles of ozone (panel **b**) and water vapour (panel **c**) retrieved from ACS MIR, and temperature retrieved from ACS NIR (panel **d**). Colours indicate L_s. These profiles were measured at middle southern latitudes (55°S-66°S) during the aphelion period (southern winter) and correspond to Figures 2**g**.

We observe around 200 ppbv O_3 in the lowest layers of the atmosphere, from 15 km to the surface, before L_s = 120°. This rapidly falls off towards 20 km, to undetectable levels above 30 km, consistent with observed increases in H_2O VMR from 1 to 5 ppmv at those altitudes. The O_3 enhancement seen at 30 km occurs during a time period in which Montmessin & Lefèvre (2013) reported a layer of O_3 over the south polar region (70°S-80°S) and attributed it to poleward transport of oxygen. Our observations are restricted to higher latitudes, and those early profiles in Figure 4**b** are the northern-most in this data set (towards to 55°S) and more likely related to aphelion cloud belt formation (discussed below).

A portion of the O_3 profiles shown in Figure 4**b** have consistently higher VMRs (brighter green to yellow colours). These are from the latest time period in this grouping and were generally recorded at further southern latitudes as well (brighter yellow colours in Figure 2**g** also). To show this, Figure 4 is reproduced as Figure S2 with the profiles coloured by latitude. For these late southernmost profiles, we observe also the coldest temperatures in the lower atmosphere, combined with warmer temperatures above 30 km. This results in the largest H_2O VMRs above 30 km, but also the largest H_2O VMR gradient and nearly no detectable water vapour below 25 km, allowing for higher ozone abundances.

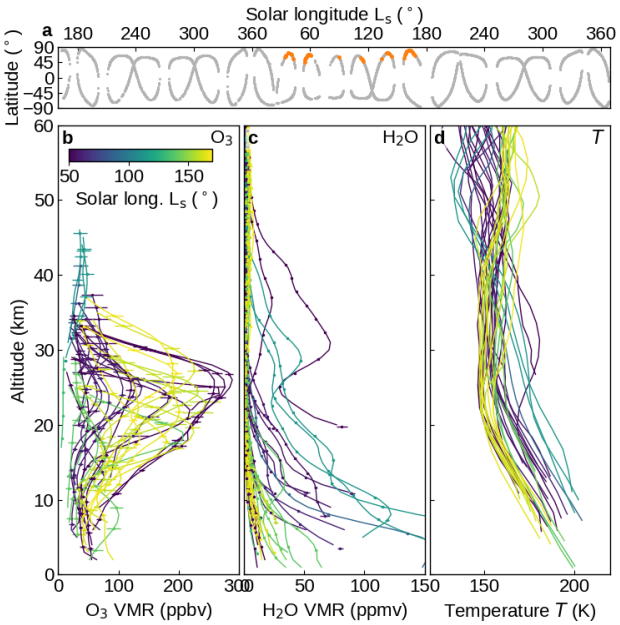

Figure 5. Aphelion ozone observations during northern late spring and summer. Panel **a** shows the latitude and L_s of observations, VMR vertical profiles of ozone (panel **b**) and water vapour (panel **c**) retrieved from ACS MIR, and temperature retrieved from ACS NIR (panel **d**). Colours indicate L_s. These profiles were measured at northern latitudes (55°N-66°N) during the aphelion period (northern summer) and correspond to Figure 2**c**.

During the same time period, but in the northern hemisphere, we observed similarly cold temperatures around 20-30 km, resulting in low water vapour abundances and allowing ozone to accumulate. In contrast to the south, the lower atmosphere is warmed by northern summer, creating a layer of water vapour near the surface, and depleting ozone below 20 km. These profiles are shown in Figure 5 and correspond to Figure 2**c**. Most observations in which ozone was observed occurred towards the start (dark blue colours) or end (yellow colours) of this season. Towards the midpoint, ozone abundances are low, corresponding to increased water vapour and the highest temperatures. These endpoints are closely related to ozone activity occurring near the equinoxes. During the middle of this period the atmosphere is sufficiently warm to host water vapour, leading to ozone depletion.

Stellar occultation and nadir observations made by SPICAM have been able to show that there are unique mechanisms impacting ozone abundance over the poles during the winter polar nights. SPICAM O_3 vertical profiles during the southern polar winter were compared with GCM simulations to show that transport of high-altitude oxygen-rich air from sunlight regions leads to an ozone layer forming at 50 km (Montmessin & Lefèvre, 2013). Integrated column abundances, combined with GCM simulations, have shown that H_2O photolysis is no longer responsible for O_3 destruction near the surface (Lefèvre et al., 2021). ACS MIR solar occultations during the perihelion period covering northern winter are not able to verify these mechanisms, however, since they are restricted further south, to the sunlight regions of Mars.

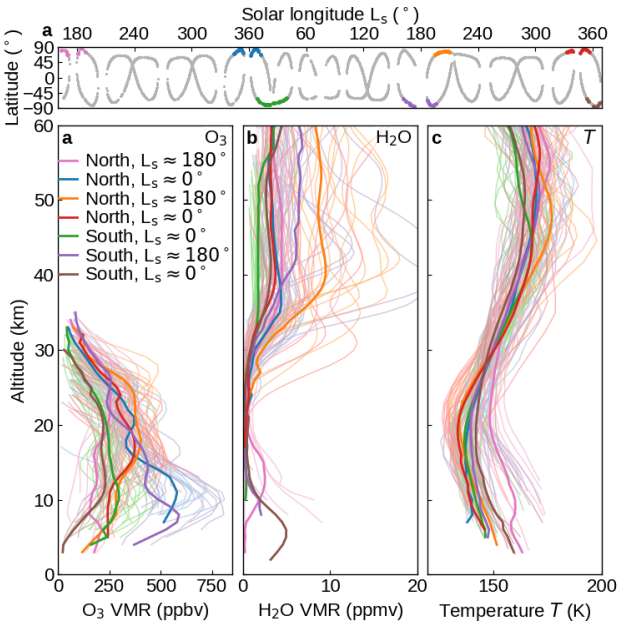

Figure 6. Ozone observations during the equinoctial periods. Panel **a** shows the latitude and L_s of observations, VMR vertical profiles of ozone (panel **b**) and water vapour (panel **c**) retrieved from ACS MIR, and temperature retrieved from ACS NIR (panel **d**). Colours indicate grouping by time period and hemisphere. These profiles were measured towards the north and south poles around L_s 0° and 180° and correspond to panels **b**, **d**, **e**, **f**, **h** and **i** of Figure 2.

TGO solar occultation opportunities probe the furthest towards the poles during the equinoxes when the plane of Mars' axial tilt is perpendicular to the sun, and it is neither polar night nor day. The vernal and autumnal equinoctial periods in the north and south that surround the aphelion periods have been combined and are shown in Figure 6. As expected, the periods between seasons indicate a symmetric atmosphere north and south. Figure 6 combines vertical profiles from high northern and far southern latitudes around both the vernal and autumnal equinoxes (panels **a**, **b**, **d**, **e**, **f**, **h** and **i** of Figure 2). These periods are characterised by a cold lower atmosphere, increasing from ~140 K near 20 km to ~165 K above 45 km. Temperatures below 35 km are consistently lower during the equinoxes than those shown in Figure 4**d** from the southern winter.

Below 30 km, water vapour abundances rapidly fall, revealing a dry lower atmosphere at these near-polar latitudes (it is near the equinoxes that ExoMars solar occultations probe nearest the poles due to the axial tilt being perpendicular to the Sun-Mars axis). This dry, cold, polar lower atmosphere provides conditions for O_3 to remain in the atmosphere, and we consistently record around 200-500 ppbv O_3 from 25 km to the surface.

Around the equinoxes, Lefèvre et al. (2021) noted a significant difference between the retrieved ozone columns in the northern spring (L_s = 0-30°) and northern autumn periods (L_s = 150-180°) using data from SPICAM. This was also visible in the LMD GCM simulations. ACS MIR vertical profiles are able to show why there was a difference in the column abundances between the spring and autumn observations. In Figure 6, we show that the equinoctial periods near L_s = 0° and L_s = 180° have very similar VMR magnitudes and vertical profile shapes. However,

the period L_s = 150-180° identified by Lefèvre et al. (2021) is too early in this season to exhibit such symmetric behaviour. ACS MIR profiles from it are included in Figure 2**a** and **c** (and 5**a**). In contrast to the profiles shown in Figure 2**d** (and 6**a)**, which feature ~400 ppbv O_3 between 10-25 km, the profiles from before L_s = 180° exhibit a sharp decline in O_3 abundance below 25 km. This is due to the late-season persistence of the low-altitude H_2O layer in northern summer (see Figure 5). In the SPICAM data, the period following L_s = 180° also has low column abundances, but matches those obtained at low southern latitudes, which are in agreement with ACS MIR results that show north-south symmetry at this time. During L_s = 0-30°, SPICAM coverage extends north over the polar vortex region, at the end of a period in which the polar O_3 layer is fully formed and confined below 5 km. Conversely, during L_s = 180-210°, the SPICAM coverage is pushed southward, to the periphery of the polar region and at a time when the polar ozone layer has not yet fully formed. Due to the similarity in ACS MIR profiles from these periods (Figures 2**a**, **c**, and **e**), it is likely that the difference in latitude coverage and the behaviour of O_3 below 5 km is responsible for the discrepancy in column abundances.

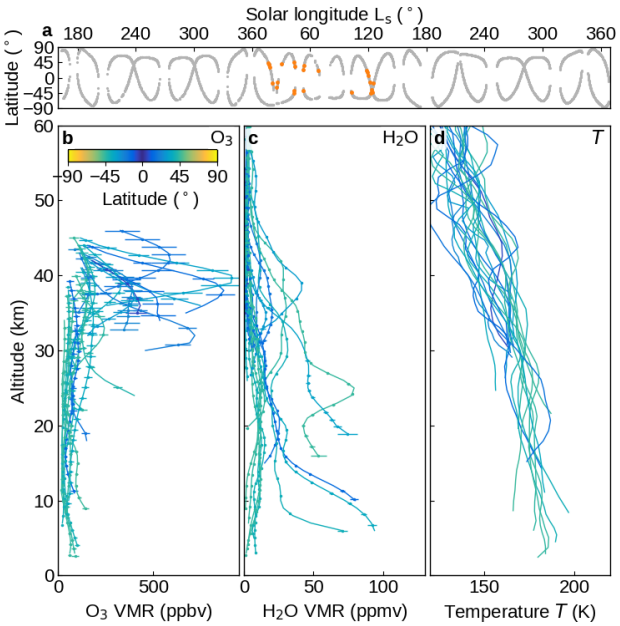

Figure 7. Ozone observations made in the equatorial region during the aphelion period. Panel **a** shows the latitude and L_s of observations, VMR vertical profiles of ozone (panel **b**) and water vapour (panel **c**) retrieved from ACS MIR, and temperature retrieved from ACS NIR (panel **d**). Colours indicate latitude. These profiles were measured at low latitudes (40°S-40°N) during the aphelion period (southern winter/northern summer) and correspond to panels **c** and **g** of Figure 2.

A unique grouping of observations is during the aphelion period, but at latitudes towards the equator in both hemispheres, between 40°S and 40°N. Compared to the other case studies presented here, observations in this period feature a unique temperature profile exhibiting a uniform gradient from a warm surface (~180 K) to a very cold upper atmosphere (< 130 K at 60 km), shown in Figure 7**c**. This temperature gradient allows for water vapour of varying abundances to be present below 30 km, but only in trace amounts above (Figure 7**b**). At these times and latitudes, when ozone is observable, we note very low abundances below 30 km,

which are the only altitudes we otherwise detect ozone in our data. Uniquely, we observe enhancements of ozone of several 100 ppbv at 40 km (Figure 7**a**).

The change in water vapour abundance at these times and latitudes is due to condensation and is caused by the temperature gradient. This also results in the formation of the well known aphelion cloud belt (Clancy & Nair, 1996; Pearl et al., 2001; Smith, 2004), and was observed by SPICAM (Lebonnois et al., 2006). In an ACS MIR solar occultation sequence of spectra, the impact of aerosol attenuation can be seen as a reduction in transmission level towards lower altitudes. At certain wavelengths, retrieving aerosol properties and identifying ices and dust can be accomplished when analysing the continuum in the transmission whose shape is solely determined by the particulate components and their broad spectral features (Luginin et al., 2020; Stcherbinine et al., 2020). During the aphelion period and the equinoctial periods (Figures 2, 5, and 6) attenuation occurs below 10 or 20 km. Over the equatorial region during the aphelion period (Figure 7), however, we consistently see attenuation beginning around 40 km, corresponding to the fall in H_2O VMR at colder temperatures.

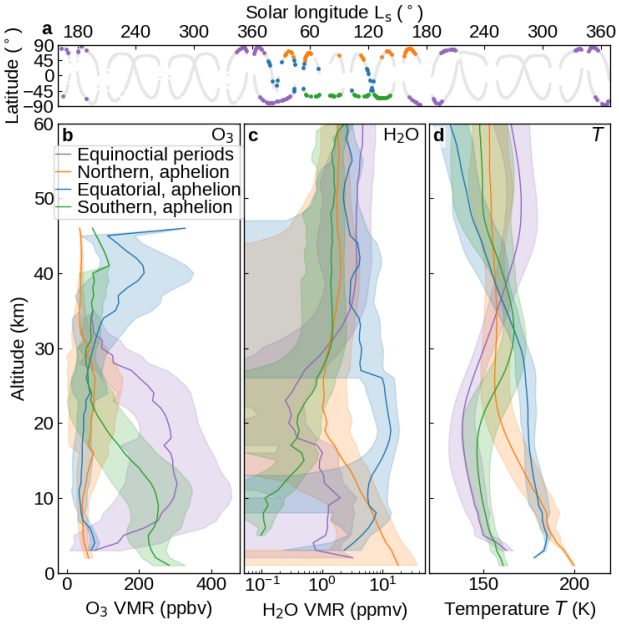

Figure 8. Mean vertical profiles of ozone and water vapour VMRs and temperature from the equinoctial periods (Figure 6), and over the aphelion period in the northern hemisphere (Figure 5), the equatorial region (Figure 7), and the southern hemisphere (Figure 4). The shaded regions indicate one standard deviation of the averaged profiles.

Figure 8 summarises these results by taking the collected profiles in Figure 4-7 and showing their means and standard deviations. During the perihelion period, in which it is summer in the southern hemisphere and dust activity is highest, we are unable to observe ozone at any southern latitudes, and make only occasional observations in the northern hemisphere of low quantities (<200 ppbv) of O_3 below 20 km (around 50°N). In the aphelion period, during northern summer, we are able to observe O_3 below 30 km, but it is strongly reduced at the lower altitudes due to increasing temperatures and water vapour towards the surface. In southern winter, we make frequent and consistent observations of >100 ppbv O_3 from between 20-30 km to the surface.

Between seasons, around both equinoxes in both hemispheres, we observe north-south symmetry in the atmosphere and the highest ozone abundances from 30 km towards the surface.

The comparison is made between O_3 VMR, H_2O VMR and temperature. Temperature controls the condensation of water vapour. Gaseous water vapour photolysis leads to HO_2 formation which converts odd-oxygen to stable O_2, effectively reducing O_3 concentrations. The production of O_3 at these altitudes, from CO_2 photolysis should otherwise be stable due to the stability of CO_2 concentrations and it being well-mixed. Therefore, the observed changes in O_3 VMRs with latitude and season are the result of changes in its loss rate, directly related to temperature and the VMR of water vapour. Note that CO_2 is only well mixed until 70-120 km (depending on latitude), above which its photolysis rate increases dramatically, leading to enhanced production of CO and O (Olsen, Lefèvre, et al., 2021), which are transported poleward and downwards leading to ozone production (Montmessin & Lefèvre, 2013), but such latitudes (polar night) and altitudes (50 km) are not investigated here.

Notably, the highest abundances of O_3 observable by ACS MIR above 30 km (equatorial aphelion, Figure 7) correspond to the coldest observed temperatures at those altitudes. The warmest period is the southern and northern hemispheres around perihelion, and corresponds to when O_3 is difficult to detect and abundances are low. The periods with the highest O_3 VMRs correspond to those in which the lower atmosphere is coldest (equinoctial and southern aphelion, Figures 6 and 4). While the anti-correlation between H_2O and O_3 was anticipated, this is the first direct comparison between the vertical profiles of temperature and the abundances of those two species, revealing the direct impact climate has on odd-hydrogen and odd-oxygen in the Martian atmosphere over different altitudes.

5 O_3 modelled by the LMD GCM

The behaviour of ozone in the Martian atmosphere has been well reproduced by contemporary GCMs. Previous efforts using the LMD GCM have shown it can reproduce SPICAM observations through modelled transport and photochemistry (Montmessin & Lefèvre, 2013) and the GEM-Mars GCM has been compared to CRISM (Compact Reconnaissance Imaging Spectrometer for Mars) and NOMAD data (Daerden et al., 2019). However, comparisons with both models to vertical profiles measured with TGO instruments have revealed a discrepancy between the magnitude of modelled and retrieved O_3 VMRs, despite good agreement in O_3 distribution and variability (Khayat et al., 2021; Olsen et al., 2020; Patel et al., 2021).

Lefèvre et al. (2021) noted that the LMD GCM underestimated O_3 column abundances by about 2 times, and that the strong difference between northern spring and summer was not reproduced. However, after the inclusion of heterogeneous uptake of OH, HO_2 and H_2O_2 on water ice aerosols was included, these differences were largely overcome, but only at high northern latitudes during the aphelion period (spring and summer). This indicates a strong dependence of O_3 on aerosol formation, and thus temperature, as we have observed with ACS MIR, especially related to the aphelion cloud belt.

We use here the latest version of the LMD Mars GCM (Forget et al., 1999) with comprehensive chemistry as described by Lefèvre et al. (2021). The atmosphere has been modelled at local terminator times, taking into account the insolation at the ACS MIR solar occultation points. Included are dust transport and radiative feedback (Madeleine et al., 2012), water vapour and

cloud physics (Navarro et al., 2014), and O_3 and CO photochemistry (Lefèvre et al., 2008). The accuracy of the GCM for a specific Mars year depends on constraints from prescribed climatologies (while dust is transported, its column abundance is forced to follow observations) and this run uses ultraviolet solar flux from González-Galindo et al. (2015) and dust climatologies for MY 34 and 35 computed as described by Montabone et al. (2015, 2020).

Climatologies of O_3 in both hemispheres predicted by the LMD GCM are shown in Figure 9 where at each ACS MIR solar occultation latitude and L_s, vertical profiles of temperature and the VMRs of O_3 and H_2O were extracted from the model at the true local solar time of terminator crossing. The main features observed by ACS are reproduced by the model. Figure 2 has been reproduced using LMD GCM output in Figure S1 for reference.

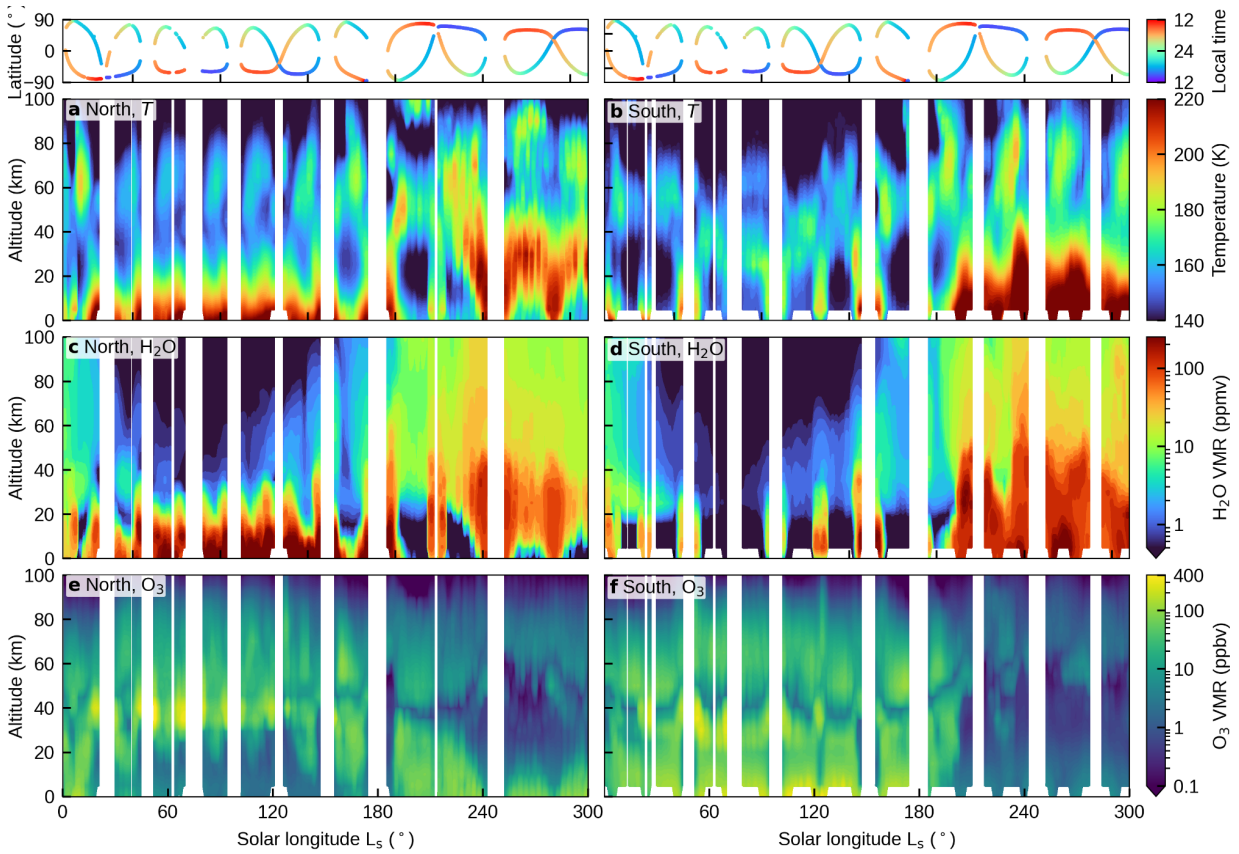

Figure 9. Vertical profiles of temperature, water vapour VMR and ozone VMR produced by the LMD GCM for local terminator times of ACS MIR solar occultations in MY 35. The data are organised by L_s but represent a range of latitudes that depend on the TGO orbit. The top panels indicate the changing local times and latitudes of ACS MIR solar occultations. Panel **a** shows temperatures in the northern hemisphere; **b** temperatures in the southern hemisphere; **c** water vapour VMRs in the northern hemisphere; **d** water vapour VMRs in the southern hemisphere; **e** ozone VMRs in the northern hemisphere; **f** ozone VMRs in the southern hemisphere. Data are averaged in 1° L_s bins.

During the perihelion period, very low O_3 VMRs are predicted (~ 0.5 ppbv), especially in the southern hemisphere (summer). In the northern hemisphere, O_3 is depleted between 20-50 km,

but remains at lower altitudes (50-100 ppbv) and high latitudes where it is winter over the polar region and cold surface temperatures cause water vapour to condense out of the atmosphere. The scarcity of O_3 observations by ACS MIR at this time indicates that the polar vortex in the GCM may extend further south than we are observing.

Higher O_3 VMRs (100-200 ppbv) are computed during the aphelion with ozone prevalent up to and above 80 km. In the southern hemisphere, throughout the aphelion period, an ozone layer forms in the lower atmosphere around 30 km that increases from ~30 ppbv to 50-80 ppbv and is observed from before the autumnal equinox to after the vernal equinox. The difference in low altitude ozone concentrations between north (< 10 ppbv) and south (50-140 ppbv) is due to the availability of water vapour in the north, as shown with the ACS MIR data in Figures 4 and 5, and supported by the model in Figure 9**c**. A second ozone layer (20-30 ppbv) centred at 50 km is also present throughout this time frame in both hemispheres. This is above the effective altitude range of ACS MIR observations of O_3 in the mid-infrared, but has been observed by other instruments (Khayat et al., 2021; Lebonnois et al., 2006; Patel et al., 2021).

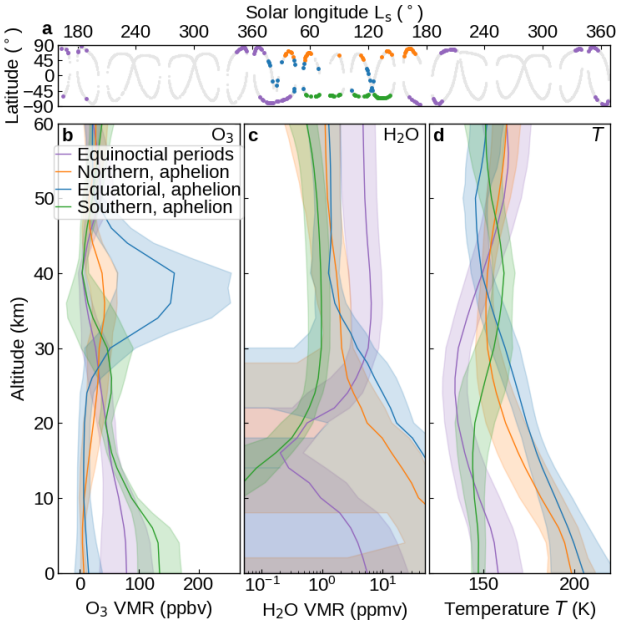

Figure 10. Mean vertical profiles extracted from the LMD GCM. Shown are ozone VMR in panel **b**, water vapour VMR in panel **c**, and temperature in panel **d**, as in Figure 8. Each profile was modelled at the local solar terminator time and location of an ACS MIR solar occultation. Profiles are grouped into the equinoctial periods (Figure 6), and over the aphelion period in the: northern hemisphere (Figure 5), the equatorial region (Figure 7), and the southern hemisphere (Figure 4). The shaded regions indicate one standard deviation of the averaged profiles.

The aphelion ozone layer at 40 km that we observe during the equatorial crossings is also predicted by the model (50-300 ppbv), and is visible in both hemispheres in Figure 9 when latitudes move away from the poles. These are visible near L_s 15°, 50°, 100°, 125°, and 150°. This peak is also shown in the individual profiles in Figure S1. Thus, the model and observation concur on the presence of a three layer structure for ozone, with enhancements at the surface, near 40 km, and again above 50 km. The magnitudes of each enhancement are latitude dependent

and more readily observed during aphelion. The surface and mid-altitude layers are not formed by additional ozone production, however, and the southern aphelion period represents the production rate of O_3 from oxygen recombination ($O_2 + O$) related to the photolysis of CO_2 that should be relatively constant with latitude, altitude, and season, controlled by CO_2 concentrations and solar flux. The layer structure that we have observed, and that is predicted by the model, is created by changes in the rate of odd-oxygen removal controlled by water vapour variability.

At an altitude near 40 km during the cold and dry aphelion period, a warm layer with a corresponding enhancement of water vapour is apparent (Figure 9**b** and **d**). This feature is visible in the modelled temperature and water vapour is also seen in ACS NIR observations (Fedorova et al., 2020). This feature appears at the same time, altitude and latitudes where O_3 is observed to decrease rapidly, (Figure 9). The high-altitude (50 km) and surface ozone layers observed by ExoMars at mid-latitudes (45°-65°) (Khayat et al., 2021; Patel et al., 2021) are likely connected by similar rates of ozone production from CO_2 photolysis. The formation of two separate layers is likely caused by changes in the destruction rate due to odd-hydrogen at 40 km, rather than excess O_3 production above 50 km, either due to transport or photochemistry.

Rather than considering the entire climatologies of ozone, water vapour, and temperature, Figure 10 shows the mean profiles extracted from the GCM at only the ACS MIR observations, reproducing Figure 8. The different trends seen in each seasonal and latitudinal grouping are clearly visible. In Figure 10**a**, we see that the average ozone VMRs in the GCM are about half those observed, with the magnitudes around the equinoxes and at southern latitudes being around 100 ppbv. ACS MIR observations are >200 ppbv and extend to higher altitudes. The O_3 abundances modelled by the GCM over southern winter are greater than those from the equinoxes, in contrast to ACS MIR observations. Another notable difference is that around northern summer (aphelion) O_3 extends to much higher altitudes in the GCM than the observations. The equatorial ozone layer is very prominent in the GCM data, and the magnitudes of the GCM and the observations are in good agreement, with mean VMRs reaching 200 ppbv.

The magnitudes of low-altitude water vapour also exhibit differences between the GCM and observations. The northern and equatorial regions around aphelion reach ~100 ppmv in the GCM, while ACS MIR observations only revealed ~50 ppmv. The profile shapes are well reproduced, as are the VMRs above 10 km. The temperature profiles exhibit the same shapes and magnitudes (Figures 8**c** and 10**c**), with the low-altitude temperatures much warmer in the equatorial and northern regions over the aphelion period (northern summer) than in the south or around the equinoxes. The altitude at which a transition occurs (warming or cooling above 30 km) is higher in the GCM in each case.

Figure 11 shows a direct quantitative comparison of ACS MIR retrievals and profiles extracted from the GCM. For each occultation, the vertical profiles from the GCM were interpolated to the pressure levels of the ACS MIR tangent heights where ozone was found. Pressure levels are used rather than tangent heights to mitigate any errors between the estimated heights of ACS MIR and ACS NIR. The comparison is done using number densities rather than VMRs since differences in retrieved VMR may result from differences in temperature and pressure (number density), rather than measured absorption line depths. The three panels in Figure 11 show a comparison between the GCM results and water vapour retrieved with ACS MIR data, ozone VMR retrieved with

ACS MIR data, and temperature retrieved using ACS NIR data (Fedorova et al., 2020). The colours are used to group occultations by the latitude and season, as in Figures 4-8.

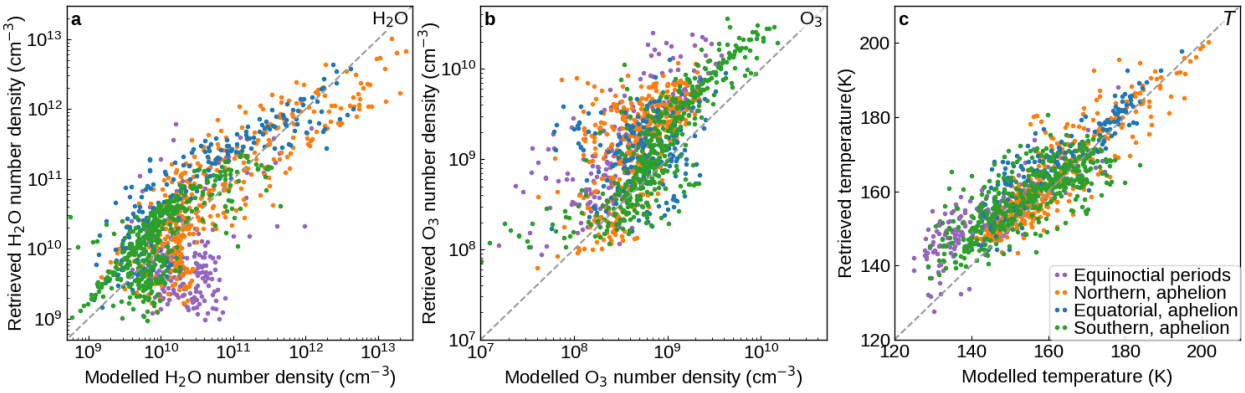

Figure 11. Comparison of H_2O, O_3, and temperature retrieved from ACS data and computed by the LMD GCM. Each retrieved tangent height where O_3 retrievals were made in an occultation sequence are shown. Pressure levels of the profiles extracted from the LMD GCM are interpolated to those of ACS tangent heights. Panels show: **a** H_2O number density retrieved from ACS MIR and modelled by the LMD GCM; **b** O_3 number density retrieved from ACS MIR and modelled by the LMD GCM; **c** temperature retrieved from ACS NIR (Fedorova et al., 2020) and modelled by the LMD GCM. Dashed grey lines indicated one-to-one correlation. Colours indicate groupings of latitude and season.

In figure 11**a** we see good agreement between water vapour retrieved from ACS MIR and modelled by the GCM, with data generally not showing a bias above or below the line of unity, except during the equinoctial periods. At those times, we are observing less water vapour than the model predicts. Since the pressure range for the comparison comes from the ozone retrievals, these data are restricted to the lower atmosphere, where temperatures and water vapour VMRs were among the lowest measured in this study (Figure 8). The profiles extracted from the LMD GCM reveal a similarly low H_2O VMR with a sharp decrease in water vapour occurring at ~15 km. However, the LMD GCM predicts larger VMRs above 30 km (> 5 ppmv compared to < 2 ppmv with ACS MIR) and a more prominent surface layer of water vapour, causing the VMR to increase again below 10 km.

Figure 11**b** shows the number density of ozone retrieved from ACS MIR data and compared to the GCM. ACS MIR generally observes higher ozone concentrations than predicted by the GCM. This tends to occur in each latitude and L_s grouping (but notably so in the equinoctial periods, related to the difference in water vapour described above). The difference tends to be on the order of 2-6 times greater, in agreement with previous studies (e.g., Lefèvre et al., 2021; Olsen et al., 2020; Patel et al., 2021). The closest agreement occurs in the southern hemisphere around aphelion (1-2 times the GCM). Periods with larger differences are equinoctial periods (~4 times) and in the north, around aphelion (~6 times).

The third panel of Figure 11 shows a comparison between LMD GCM temperature profiles and those retrieved using ACS NIR. These are discussed in Fedorova et al. (2020). In general, we observe warmer temperatures in the lower atmosphere, but not in a way that systematically

impacts observations of water vapour, which would lead to lower ozone abundances than observed.

6 Relationships between O_3, H_2O, and temperature

Direct comparisons of the column abundances of O_3 and H_2O measured with SPICAM over four Martian years have been used to quantify the anticorrelation between these species (Lefèvre et al., 2021). SPICAM viewing geometry allows for observations of polar summers, but not winters, and the best agreement in latitudinal coverage between SPICAM and ACS MIR is around the equinoxes when ACS MIR observations extend the furthest poleward. Therefore, their coverage is greatest at high northern latitudes (>60°N), and distinct trends are observed at different time periods, with a stronger reduction in O_3 relative to H_2O observed during northern summer (L_s 60°-150°) than in the spring or equinoxes. The O_3 column abundance relative to H_2O is smaller in the southern hemisphere, although there is symmetry about the autumnal equinox. Coverage is limited in the south because polar winter is not observed and O_3 column abundances in summer are at the detectable limits (< 0.5 μm-atm). No correlation was observed at mid-latitudes. The nadir SPICAM observations used to derive column abundances are most sensitive to the lowest layers of the atmosphere and the vertical profiles produced by ACS MIR are able to provide more information about the behaviour of O_3 and H_2O at the different periods observed.

The accuracy, vertical resolution, and sensitivity to temperature, pressure, and multiple trace gases of ACS provide a unique opportunity to probe the relationship between different chemical species. The anti-correlation of ozone and water vapour was noted qualitatively in early observations and repeatedly confirmed (e.g., Clancy et al., 1996; Lefèvre & Krasnopolsky, 2017; Perrier et al., 2006 and references therein) and quantified using SPICAM nadir data (Lefèvre et al., 2021). Figure 12 shows the correlation between retrieved water vapour VMRs and retrieved ozone VMRs for the coincident measurements made with ACS MIR at each altitude where ozone was observed. Panels **a** and **b** both contain the same data, with panel **a** showing the uncertainties of the retrieved data and the density of the observations, and panel **b** using colours to indicate the latitude and L_s groupings. A large scatter is revealed by these plots, but the density of the data (Gaussian kernel density estimate) shows that the majority falls along a straight line indicating an exponential relationship between the VMRs of both gases, and that small amounts of water vapour lead to rapid depletion of ozone.

The anti-correlation is not always verified. There is a cluster of data with <50 ppbv O_3 and ~1 ppmv H_2O. This is visible in the data collected in the south during aphelion. There, observations made near 20 km feature overlapping altitude regions with strong gradients in the O_3 and H_2O abundances, where ozone is declining and water vapour rapidly increases as altitude grows (Figure 4). Ozone in this period is only observed at low altitudes, around 10 km, and the water vapour is observed to fall rapidly between 20 and 10 km. A third unique set of observations is that of the equatorial aphelion ozone layer. As water vapour abundance falls and the ozone VMR increases, an apparent minimum water vapour VMR is reached (around 1 ppmv), while the ozone concentration continues to increase above 200 ppbv.

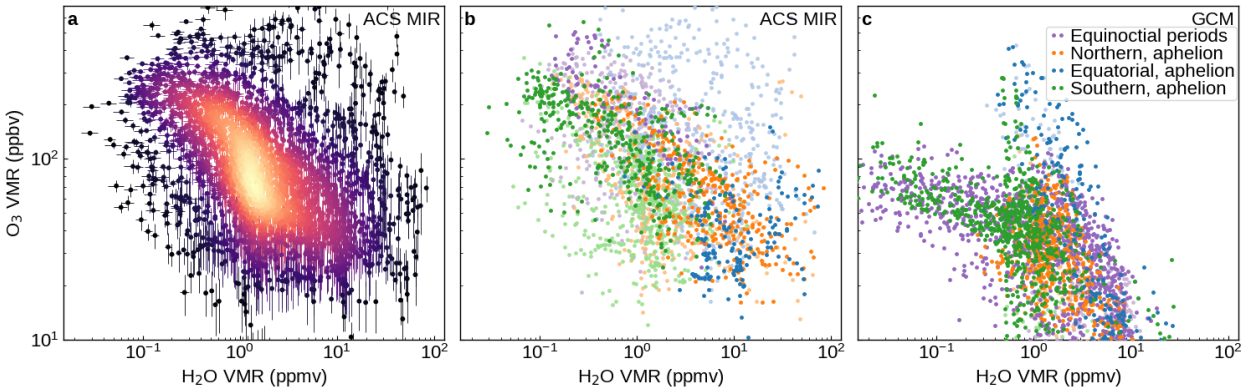

Figure 12. Correlation between water vapour and ozone. Panels **a** and **b** show the simultaneous retrieved O_3 and H_2O data at each tangent height, where both gases were measured by ACS MIR. Panel **a** includes measurement uncertainties and is coloured using a Gaussian kernel density estimate (brighter means high density of data points). Panel **b** shows the same data as panel **a**, but using colours to indicate the latitude and L_s groupings used in Figures 4-8. Bold colours indicate altitudes below 20 km, while faint colours indicate data above 20 km. Panel **c** uses vertical profiles of H_2O and O_3 VMRs extracted from the LMD GCM for the terminator times at the latitude and L_s of the ACS MIR occultations used in panels **a** and **b** (coloured as in panel **b**).

The data in Figure 12**b** are distinguished by lighter and darker colours to show whether they are from altitudes above 20 km or below. When only the lower altitudes are considered, excluding the altitude range where both O_3 and H_2O are changing relative to one another, the anti-correlation is much tighter.

While the overall anti-correlation is visible in the density plot of the data, the wide variability due to changes in O_3 and H_2O VMRs over altitude, combined with differences between each of the L_s groups leads to low Pearson correlation coefficients, which range from -0.29 to -0.35. Another aspect that affects the anti-correlation that can be explored in the future using a GCM is the impact of local dynamics which would perturb the O_3 and H_2O abundances.

Figure 12**c** shows the same thing, but using the vertical profiles of H_2O and O_3 VMR extracted from the LMD GCM at the latitude and L_s of the ACS MIR occultations. The anti-correlation between water vapour and ozone reveals a similar exponential trend, but with much less ozone being present (and thus a lower slope in panel **c**), by a factor of >2 when considering the maximum values along the trend being ~100 ppbv for the GCM and ~200 ppbv for ACS MIR measurements. This confirms the results from SPICAM (Lefèvre et al., 2021). This is consistent with the differences between model and observation shown in Figure 11. Of note is that there remains a cluster of data related to the southern aphelion, with VMRs of H_2O ~1 ppmv and O_3 < 100 ppbv. These are related to altitudes where increasing water vapour profiles overlap with decreasing ozone profiles. Such cases were noted to be the cause of differences between the model and observation during the equinoctial periods as well.

A second feature that deviates from the trend is the data from the equatorial observations. In the model data, the ozone data climbs to well over 300 ppbv, but does so in the presence of constant ~1 ppmv of water vapour, unlike other time periods where >100 ppbv of ozone was observed. This agrees with the observations.

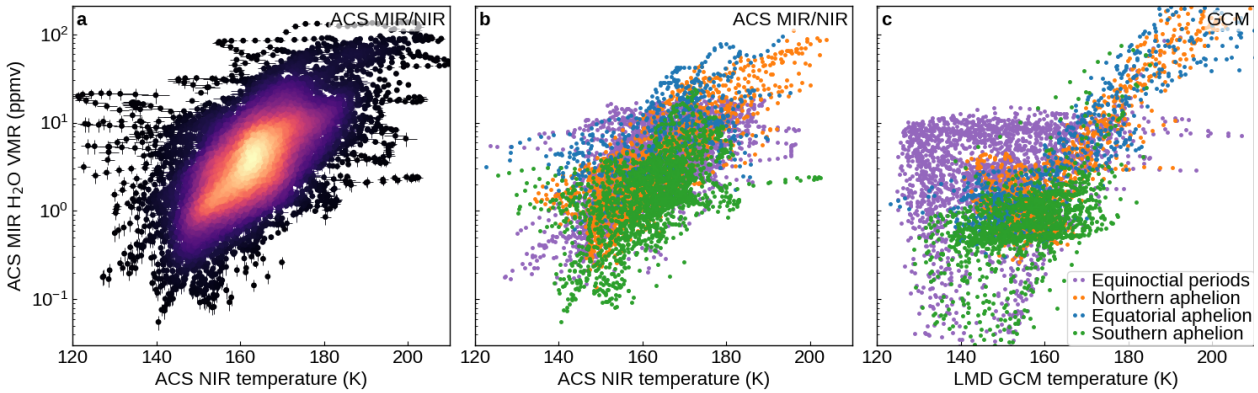

Figure 13. The correlation between water vapour and temperature. Panels **a** and **b** show the retrieved H_2O from ACS MIR and the coincident measurements of temperature made with ACS NIR. The ACS NIR data was interpolated to the pressure levels of the ACS MIR tangent heights. Panel **a** includes measurement uncertainties and is coloured using a Gaussian kernel density estimate (brighter means high density of data points). Panel **b** shows the same data as panel **a**, but using colours to indicate the latitude and L_s groupings used in Figures 4-8. Panel **c** uses vertical profiles of H_2O and O_3 VMRs extracted from the LMD GCM for the terminator times at the latitude and L_s of the ACS MIR occultations used in panels **a** and **b** (coloured as in panel **b**).

In our discussion of Figure 8, we noted that the shape of the ozone profiles appeared to be related to the temperature of the atmosphere, via the condensation of water vapour. Figure 13 shows the correlation between water vapour retrieved using ACS MIR data and the measured temperature profiles from ACS NIR (Fedorova et al., 2020). A positive correlation is seen between the two measured quantities, with water vapour increasing exponentially with positive changes in temperature. We note that the rate of change of water vapour is found to be lower during the northern perihelion, corresponding to the warmest and wettest conditions presented here. Another unique set of observations is again the equatorial period in which a minimum amount of water remains in the atmosphere while temperatures decrease towards some of the coldest temperatures presented here, occurring above 40 km.

Figure 13**c** again shows the same correlation data, but using profiles extracted from the GCM. The GCM reveals a similar trend to the data, with the same groups of outliers. Over the equatorial observations, we see a change in the trend as temperatures fall below 150 K. The southern aphelion data is tightly clustered, as it was when comparing ozone to water vapour in Figure 12, but this time the retrieved data is less clustered than the GCM data. A major difference comes from the equinoctial period observations. In the GCM, descending from 50 km, the temperatures fall from ~180 K to ~140 K, while the H_2O VMRs tend to be fairly constant. From around 30 km towards the surface, temperatures increase again, but the water vapour falls off very rapidly by 20 km due to the cold temperatures. Similar behaviour is observed in the retrievals, but to a lesser extent. A difference between the model data and the retrievals impacting this comparison is that the minimum atmospheric temperature occurs at a lower altitude in the ACS NIR data than in the model computations.

7 Conclusions

We present here three years of data collected by ACS MIR on the ExoMars TGO, covering the second half of MY 34, all of MY 35, and the start of MY 36. ACS MIR operating in solar occultation mode is sensitive enough to measure vertical profiles of the VMR of O_3 using the infrared 003←000 absorption band (3000-3060 cm^{-1}). By comparing the vertical structure of simultaneously measured ozone, water vapour, and temperature, we have gleaned new insights into how these important species vary seasonally and exchange hydrogen and oxygen between them. Photochemistry in the Martian atmosphere and the stability of CO and CO_2 depend on odd-oxygen and off-hydrogen chemistry, and H_2O is the parent gas of members of the odd hydrogen family, while O_3 is an important tracer of odd-oxygen.

We have confirmed the anti-correlation between water vapour and ozone, and observed two ozone layers - a broad surface layer present during the cold and dry aphelion period, and a layer at 40 km over the equator related to the aphelion cloud band formation. Ozone is generally not observed at most latitudes in either hemisphere during the perihelion period, in which the strong southern summer creates a warm and water-rich middle atmosphere in both hemispheres. Ozone is commonly observed during southern fall and winter and northern spring and summer around perihelion, with abundances between 200-500 ppbv, which are 2-6 times larger than GCM predictions. The northern summer also hosts a near-surface water layer which causes a depletion in ozone below 20 km.

By comparing the vertical structure of ozone, water vapour, and temperature at different latitudes and time periods, we are able to see how the Martian climate controls ozone abundance by varying its rate of destruction. Cooling temperatures lead to reduction in the water vapour VMR, and thus a reduction in odd-hydrogen production, which allows O_3 to build up since odd-hydrogen is required to convert odd-oxygen into more stable molecules. The close correlations between temperature and water vapour, and between water vapour and ozone, combined with the observed differences between the expected O_3 abundances and those observed, lead us to conclude that changes in odd-hydrogen and odd-oxygen may be occurring faster than previously thought. This will have important implications for the photochemical cycles of water vapour and CO, as well as trace gases, such as HCl and methane.

Acknowledgments, Samples, and Data

The authors declare no conflicts of interest. The ACS investigation was developed by the Space Research Institute (IKI) in Moscow, and the Laboratoire Atmosphères, Milieux, Observations Spatiales (LATMOS/CNRS) in Paris. The investigation was funded by Roscosmos, the National Centre for Space Studies of France (CNES) and the Ministry of Science and Education of Russia. The GGG software suite is maintained at JPL (tccon-wiki.caltech.edu). This work was funded by the UK Space Agency (ST/T002069/1), the Natural Sciences and Engineering Research Council of Canada (NSERC) (PDF–516895–2018), and the National Centre for Space Studies of France (CNES). IKI affiliates acknowledge funding from the Russian Science Foundation (RSF-ANR 20-42-09035) (data analysis and interpretation). University of Oxford affiliates acknowledge funding from the UK Space Agency (ST/T002069/1, ST/R001502/1, and ST/P001572/1). LATMOS affiliates acknowledge funding from CNES and ANR (PRCI, CE31 AAPG2019-MCUBE project). All spectral fitting of ACS MIR data was performed by K.S.O. using the GGG software suite. Temperature and pressure data were provided by A.A.F.

Processing of ACS spectra is done by A.T. at IKI and by L.B. at LATMOS by L.B. The LMD GCM data was generated by, and provided by, F.F., E.M., F.L., and A.B. Input and aid on spectral fitting, and on interpretation of data, were given by J.A., D.A.B., C.F.W., P.G.J.I., A.F., F.M., and F.L. The ACS instrument was designed, developed, and operated by A.P., A.S., A.T., F.M., and O.K. Level 0 and Level 2B data from ACS MIR are available on the ESA Planetary Science Archive (PSA). The PSA can be accessed interactively at https://archives.esac.esa.int/psa/#!Table%20View/ACS=instrument or the ACS data can be accessed via FTP at https://archives.esac.esa.int/psa/ftp/ExoMars2016/em16_tgo_acs/data_raw/Science_Phase/. VMR vertical profiles generated in this study are available on the Oxford Research Archive at https://doi.org/10.XXXX/ (to be published on acceptance). Temperature and pressure data from ACS NIR during MY 34 are available at http://exomars.cosmos.ru/ACS_Results_stormy_water_vREzUd4pxG/.

References

Alday, J., Wilson, C. F., Irwin, P. G. J., Olsen, K. S., Baggio, L., Montmessin, F., et al. (2019). Oxygen isotopic ratios in Martian water vapour observed by ACS MIR on board the ExoMars Trace Gas Orbiter. *Astronomy & Astrophysics*, *630*, A91. https://doi.org/10.1051/0004-6361/201936234

Alday, J., Trokhimovskiy, A., Irwin, P. G. J., Wilson, C. F., Montmessin, F., Lefévre, F., et al. (2021). Isotopic fractionation of water and its photolytic products in the atmosphere of Mars. *Nature Astronomy*, *5*(9), 943–950. https://doi.org/10.1038/s41550-021-01389-x

Aoki, S., Vandaele, A. C., Daerden, F., Villanueva, G. L., Liuzzi, G., Thomas, I. R., et al. (2019). Water Vapor Vertical Profiles on Mars in Dust Storms Observed by TGO/NOMAD. *Journal of Geophysical Research: Planets*, *124*(12), 3482–3497. https://doi.org/10.1029/2019JE006109

Barth, C. A., & Hord, C. W. (1971). Mariner Ultraviolet Spectrometer: Topography and Polar Cap. *Science*, *173*(3993), 197–201. https://doi.org/10.1126/science.173.3993.197

Barth, C. A., Hord, C. W., Stewart, A. I., Lane, A. L., Dick, M. L., & Anderson, G. P. (1973). Mariner 9 Ultraviolet Spectrometer Experiment: Seasonal Variation of Ozone on Mars. *Science*, *179*(4075), 795–796. https://doi.org/10.1126/science.179.4075.795

Clancy, R. T., & Nair, H. (1996). Annual (perihelion-aphelion) cycles in the photochemical behavior of the global Mars atmosphere. *Journal of Geophysical Research: Planets*, *101*(E5), 12785–12790. https://doi.org/10.1029/96JE00836

Clancy, R. T., Wolff, M. J., James, P. B., Smith, E., Billawala, Y. N., Lee, S. W., & Callan, M. (1996). Mars ozone measurements near the 1995 aphelion: Hubble space telescope ultraviolet spectroscopy with the faint object

spectrograph. *Journal of Geophysical Research: Planets*, *101*(E5), 12777–12783. https://doi.org/10.1029/96JE00835

Clancy, R. T., Wolff, M. J., Lefèvre, F., Cantor, B. A., Malin, M. C., & Smith, M. D. (2016). Daily global mapping of Mars ozone column abundances with MARCI UV band imaging. *Icarus*, *266*, 112–133. https://doi.org/10.1016/j.icarus.2015.11.016

Daerden, F., Neary, L., Viscardy, S., García Muñoz, A., Clancy, R. T., Smith, M. D., et al. (2019). Mars atmospheric chemistry simulations with the GEM-Mars general circulation model. *Icarus*, *326*, 197–224. https://doi.org/10.1016/j.icarus.2019.02.030

Devi, V. M., Benner, D. C., Sung, K., Crawford, T. J., Gamache, R. R., Renaud, C. L., et al. (2017). Line parameters for CO_2- and self-broadening in the $^{16\$}$O. *J. Quant. Spectrosc. Radiat. Transfer*, *203*, 158–174. https://doi.org/10.1016/j.jqsrt.2017.02.020

Espenak, F., Mumma, M. J., Kostiuk, T., & Zipoy, D. (1991). Ground-based infrared measurements of the global distribution of ozone in the atmosphere of Mars. *Icarus*, *92*(2), 252–262. https://doi.org/10.1016/0019-1035(91)90049-Y

Fast, K., Kostiuk, T., Espenak, F., Annen, J., Buhl, D., Hewagama, T., et al. (2006). Ozone abundance on Mars from infrared heterodyne spectra. I. Acquisition, retrieval, and anticorrelation with water vapor. *Icarus*, *181*(2), 419–431. https://doi.org/10.1016/j.icarus.2005.12.001

Fedorova, A. A., Montmessin, F., Korablev, O., Luginin, M., Trokhimovskiy, A., Belyaev, D. A., et al. (2020). Stormy water on Mars: The distribution and saturation of atmospheric water during the dusty season. *Science*, *367*(6475), 297–300. https://doi.org/10.1126/science.aay9522

Forget, F., Hourdin, F., Fournier, R., Hourdin, C., Talagrand, O., Collins, M., et al. (1999). Improved general circulation models of the Martian atmosphere from the surface to above 80 km. *J. Geophys. Res.*, *104*, 24155–24176. https://doi.org/10.1029/1999JE001025

Gamache, R. R., Farese, M., & Renaud, C. L. (2016). A spectral line list for water isotopologues in the 1100-4100 $cm^{-1\$}$ region for application to CO_2-rich planetary atmospheres. *J. Mol. Spectrosc.*, *326*, 144–150. https://doi.org/10.1016/j.jms.2015.09.001

González-Galindo, F., López-Valverde, M. A., Forget, F., García-Comas, M., Millour, E., & Montabone, L. (2015). Variability of the Martian thermosphere during eight Martian years as simulated by a ground-to-exosphere

global circulation model. *Journal of Geophysical Research: Planets*, *120*(11), 2020–2035. https://doi.org/10.1002/2015JE004925

Gordon, I. E., Rothman, L. S., Hargreaves, R. J., Hashemi, R., Karlovets, E. V., Skinner, F. M., et al. (2021). The HITRAN2020 molecular spectroscopic database. *Journal of Quantitative Spectroscopy and Radiative Transfer*, 107949. https://doi.org/10.1016/j.jqsrt.2021.107949

Irion, F. W., Gunson, M. R., Toon, G. C., Chang, A. Y., Eldering, A., Mahieu, E., et al. (2002). Atmospheric Trace Molecule Spectroscopy (ATMOS) Experiment Version 3 data retrievals. *Appl. Opt.*, *41*, 6968–6979. https://doi.org/10.1364/AO.41.006968

Khayat, A. S. J., Smith, M. D., Wolff, M., Daerden, F., Neary, L., Patel, M. R., et al. (2021). ExoMars TGO/NOMAD-UVIS vertical profiles of ozone: Part 2: The high-altitude layers of atmospheric ozone. *Journal of Geophysical Research: Planets*, e2021JE006834. https://doi.org/10.1029/2021JE006834

Korablev, O., Montmessin, F., Trokhimovskiy, A., Fedorova, A. A., Shakun, A. V., Grigoriev, A. V., et al. (2018). The Atmospheric Chemistry Suite (ACS) of Three Spectrometers for the ExoMars 2016 Trace Gas Orbiter. *Space Science Reviews*, *214*(1), 7. https://doi.org/10.1007/s11214-017-0437-6

Korablev, O., Vandaele, A. C., Montmessin, F., Fedorova, A. A., Trokhimovskiy, A., Forget, F., et al. (2019). No detection of methane on Mars from early ExoMars Trace Gas Orbiter observations. *Nature*, *568*, 517–520. https://doi.org/10.1038/s41586-019-1096-4

Korablev, O., Olsen, K. S., Trokhimovskiy, A., Lefèvre, F., Montmessin, F., Fedorova, A. A., et al. (2021). Transient HCl in the atmosphere of Mars. *Science Advances*, *7*(7), eabe4386. https://doi.org/10.1126/sciadv.abe4386

Lebonnois, S., Quémerais, E., Montmessin, F., Lefèvre, F., Perrier, S., Bertaux, J.-L., & Forget, F. (2006). Vertical distribution of ozone on Mars as measured by SPICAM/Mars Express using stellar occultations. *J. Geophys. Res.*, *111*(E9), E09S05. https://doi.org/10.1029/2005JE002643

Lefèvre, F., & Krasnopolsky, V. (2017). Atmospheric Photochemistry. In R. M. Haberle, R. T. Clancy, F. Forget, M. D. Smith, & R. W. Zurek (Eds.), *The Atmosphere and Climate of Mars* (pp. 405–432). Cambridge University Press.

Lefèvre, F., Lebonnois, S., Montmessin, F., & Forget, F. (2004). Three-dimensional modeling of ozone on Mars. *J. Geophys. Res.*, *109*(E7), E07004. https://doi.org/10.1029/2004JE002268

Lefèvre, F., Bertaux, J.-L., Clancy, R. T., Encrenaz, T., Fast, K., Forget, F., et al. (2008). Heterogeneous chemistry in

the atmosphere of Mars. *Nature*, *454*, 971–975. https://doi.org/10.1038/nature07116

Lefèvre, F., Trokhimovskiy, A., Fedorova, A., Baggio, L., Lacombe, G., Määttänen, A., et al. (2021). Relationship Between the Ozone and Water Vapor Columns on Mars as Observed by SPICAM and Calculated by a Global Climate Model. *Journal of Geophysical Research: Planets*, *126*(4), e2021JE006838. https://doi.org/10.1029/2021JE006838

Luginin, M., Fedorova, A., Ignatiev, N., Trokhimovskiy, A., Shakun, A., Grigoriev, A., et al. (2020). Properties of Water Ice and Dust Particles in the Atmosphere of Mars During the 2018 Global Dust Storm as Inferred From the Atmospheric Chemistry Suite. *Journal of Geophysical Research: Planets*, *125*(11), e2020JE006419. https://doi.org/10.1029/2020JE006419

Madeleine, J.-B., Forget, F., Spiga, A., Wolff, M. J., Montmessin, F., Vincendon, M., et al. (2012). Aphelion water-ice cloud mapping and property retrieval using the OMEGA imaging spectrometer onboard Mars Express. *J. Geophys. Res.*, *117*, E00J07. https://doi.org/10.1029/2011JE003940

Mitchell, D. M., Montabone, L., Thomson, S., & Read, P. L. (2015). Polar vortices on Earth and Mars: A comparative study of the climatology and variability from reanalyses. *Quarterly Journal of the Royal Meteorological Society*, *141*(687), 550–562. https://doi.org/10.1002/qj.2376

Montabone, L., Forget, F., Millour, E., Wilson, R. J., Lewis, S. R., Cantor, B., et al. (2015). Eight-year climatology of dust optical depth on Mars. *Icarus*, *251*, 65–95. https://doi.org/10.1016/j.icarus.2014.12.034

Montabone, L., Spiga, A., Kass, D. M., Kleinböhl, A., Forget, F., & Millour, E. (2020). Martian Year 34 Column Dust Climatology from Mars Climate Sounder Observations: Reconstructed Maps and Model Simulations. *J. Geophys. Res.*

Montmessin, F., & Lefèvre, F. (2013). Transport-driven formation of a polar ozone layer on Mars. *Nature Geoscience*, *6*(11), 930–933. https://doi.org/10.1038/ngeo1957

Navarro, T., Madeleine, J.-B., Forget, F., Spiga, A., Millour, E., Montmessin, F., & Määttänen, A. (2014). Global climate modeling of the Martian water cycle with improved microphysics and radiatively active water ice clouds. *J. Geophys. Res.*, *119*, 1479–1495. https://doi.org/10.1002/2013JE004550

Olsen, K. S., Lefèvre, F., Montmessin, F., Trokhimovskiy, A., Baggio, L., Fedorova, A., et al. (2020). First detection of ozone in the mid-infrared at Mars: implications for methane detection. *Astron. Astrophys. in Press*. https://doi.org/10.1051/0004-6361/202038125

Olsen, K. S., Trokhimovskiy, A., Montabone, L., Fedorova, A. A., Luginin, M., Lefèvre, F., et al. (2021). Seasonal reappearance of HCl in the atmosphere of Mars during the Mars year 35 dusty season. *Astronomy & Astrophysics*, *647*, A161. https://doi.org/10.1051/0004-6361/202140329

Olsen, K. S., Lefèvre, F., Montmessin, F., Fedorova, A. A., Trokhimovskiy, A., Baggio, L., et al. (2021). The vertical structure of CO in the Martian atmosphere from the ExoMars Trace Gas Orbiter. *Nature Geoscience*, *14*(2), 67–71. https://doi.org/10.1038/s41561-020-00678-w

Olsen, K. S., Trokhimovskiy, A., Braude, A. S., Korablev, O., Fedorova, A. A., Wilson, C. F., et al. (2021). Upper limits for phosphine (PH3) in the atmosphere of Mars. *Astronomy & Astrophysics*, *649*, L1. https://doi.org/10.1051/0004-6361/202140868

Patel, M. R., Sellers, G., Mason, J. p., Holmes, J. A., Brown, M. A. J., Lewis, S. R., et al. (2021). ExoMars TGO/NOMAD-UVIS vertical profiles of ozone: Part 1 – Seasonal variation and comparison to water. *Journal of Geophysical Research: Planets*, e2021JE006837. https://doi.org/10.1029/2021JE006837

Pearl, J. C., Smith, M. D., Conrath, B. J., Bandfield, J. L., & Christensen, P. R. (2001). Observations of Martian ice clouds by the Mars Global Surveyor Thermal Emission Spectrometer: The first Martian year. *J. Geophys. Res.*, *106*, 12325–12338. https://doi.org/10.1029/1999JE001233

Perrier, S., Bertaux, J. L., Lefèvre, F., Lebonnois, S., Korablev, O., Fedorova, A., & Montmessin, F. (2006). Global distribution of total ozone on Mars from SPICAM/MEX UV measurements. *J. Geophys. Res.*, *111*(E9). https://doi.org/10.1029/2006JE002681

Smith, M. D. (2004). Interannual variability in TES atmospheric observations of Mars during 1999-2003. *Icarus*, *167*, 148–165. https://doi.org/10.1016/j.icarus.2003.09.010

Stcherbinine, A., Vincendon, M., Montmessin, F., Wolff, M. J., Korablev, O., Fedorova, A., et al. (2020). Martian Water Ice Clouds During the 2018 Global Dust Storm as Observed by the ACS-MIR Channel Onboard the Trace Gas Orbiter. *Journal of Geophysical Research: Planets*, *125*(3), e2019JE006300. https://doi.org/10.1029/2019JE006300

Trokhimovskiy, A., Perevalov, V., Korablev, O., Fedorova, A. F., Olsen, K. . S., Bertaux, J.-L., et al. (2020). First observation of the magnetic dipole CO_2 main isotopologue absorption band at 3.3 μm in the atmosphere of Mars by ACS. *Astron. Astrophys. in Press*. https://doi.org/10.1051/0004-6361/202038134

Tudorie, M., Földes, T., Vandaele, A. C., & Vander Auwera, J. (2012). CO2 pressure broadening and shift

coefficients for the 1–0 band of HCl and DCl. *Journal of Quantitative Spectroscopy and Radiative Transfer*, *113*(11), 1092–1101. https://doi.org/10.1016/j.jqsrt.2012.01.025

Waugh, D. W., Toigo, A. D., Guzewich, S. D., Greybush, S. J., Wilson, R. J., & Montabone, L. (2016). Martian polar vortices: Comparison of reanalyses. *Journal of Geophysical Research: Planets*, *121*(9), 1770–1785. https://doi.org/10.1002/2016JE005093

Wilzewski, J. S., Gordon, I. E., Kochanov, R. V., Hill, C., & Rothman, L. S. (2016). H_2, He, and CO_2 line-broadening coefficients, pressure shifts and temperature-dependence exponents for the HITRAN database. Part 1: SO_2, NH_3, HF, HCl, OCS and C_2H_2. *J. Quant. Spectrosc. Radiat. Transfer*, *168*, 193–206. https://doi.org/10.1016/j.jqsrt.2015.09.003

Wunch, D., Toon, G. C., Blavier, J. L., Washenfelder, R. A., Notholt, J., Connor, B. J., et al. (2011). The Total Carbon Column Observing Network. *Phil. Trans. R. Soc. A*, *369*, 2087–2112. https://doi.org/10.1098/rsta.2010.0240

Journal of Geophysical Research: Planets

Supporting Information for

Seasonal changes in the vertical structure of ozone in the Martian lower atmosphere and its relationship to water vapour.

K. S. Olsen[1], A. A. Fedorova[2], A. Trokhimovskiy[2], F. Montmessin[3], F. Lefèvre[3], O. Korablev[2], L. Baggio[3], F. Forget[4], E. Millour[4], A. Bierjon[4], J. Alday[1,5], C. F. Wilson[1,6], P. G. J. Irwin[1], D. A. Belyaev[2], A. Patrakeev[2], and A. Shakun[2]

[1]Department of Physics, University of Oxford, Oxford, UK.

[2]Space Research Institute (IKI), Moscow, Russia.

[3]Laboratoire Atmosphères, Milieux, Observations Spatiales (LATMOS/CNRS), Paris, France.

[4]Laboratoire de Météorologie Dynamique (LMD/CNRS), Paris, France.

[5]School of Physical Sciences, The Open University, Milton Keynes, UK.

[6]European Space Research and Technology Centre (ESTEC), Noordwijk, Netherlands

Contents of this file

Figures S1 to S2

Introduction

This supporting information for **Seasonal changes in the vertical structure of ozone in the Martian lower atmosphere and its relationship to water vapour** contains the supplementary figures S1 and S2. S1 is the same as Figure 2, but using data from the LMD GCM for comparison. Figure S2 is the same as Figure 4, but using colours indicating latitude rather than solar longitude.

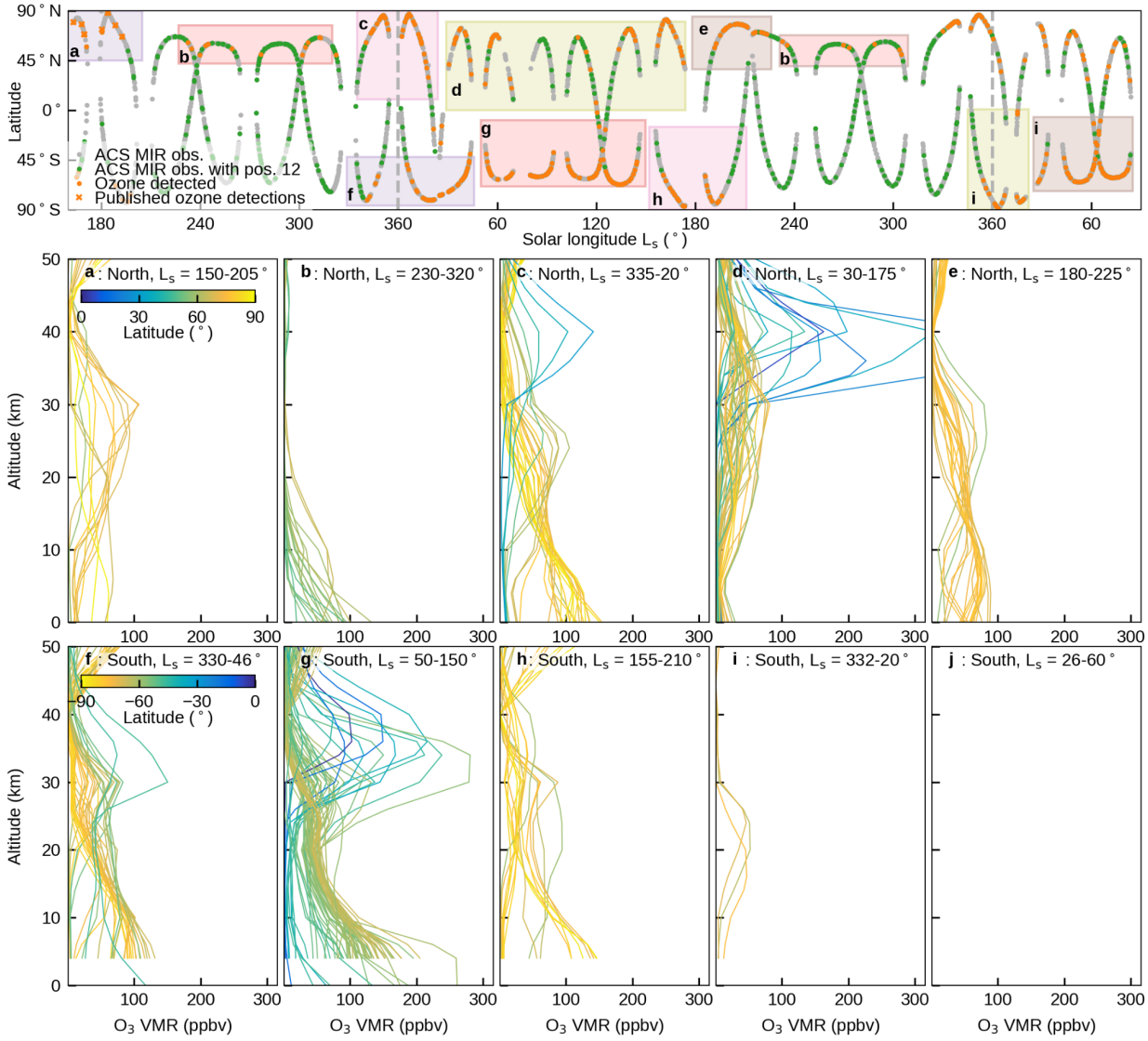

Figure S1. Vertical profiles of ozone VMR computed by the LMD GCM for comparison with ACS MIR observations. Model data is extracted for local times, L_s, and latitudes of ACS MIR solar occultation and organised as in Figure 2. Note that GCM data is only available up to the end of MY 35.

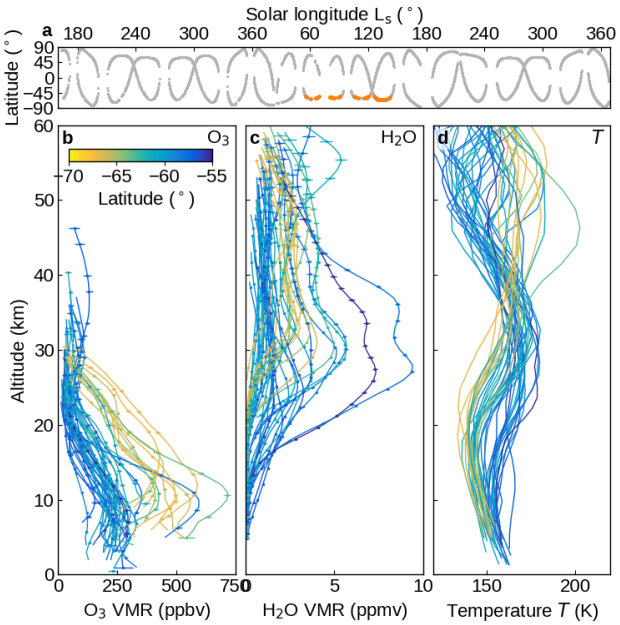

Figure S2. Ozone observations during the aphelion period. As in Figure 4 but coloured using latitudes rather than L_s. These profiles were measured at middle southern latitudes (55°S-66°S) during the aphelion period (southern winter) and correspond to Figures 2**g**.